actuators

MDPI

Article

Dynamic Analysis and Equivalent Modeling for a Four-Axle Vehicle

Dequan Zeng [1,2,3], Wei Luo [1,2], Yinquan Yu [1,2], Yiming Hu [1,2], Peizhi Zhang [3], Giuseppe Carbone [1,2,4], Dongfu Xie [1,2], Huafu Fang [1,2] and Letian Gao [3,5,*]

1 School of Mechatronics and Vehicle Engineering, Postdoctoral Research Center of Transportation Engineering, East China Jiaotong University, Nanchang 330013, China; 3340@ecjtu.edu.cn (D.Z.); 2022038085500084@ecjtu.edu.cn (W.L.); yu_yinquan@ecjtu.edu.cn (Y.Y.); 3314@ecjtu.edu.cn (Y.H.); giuseppe.carbone@unical.it (G.C.); 3278@ecjtu.edu.cn (D.X.); 2022038080200029@ecjtu.edu.cn (H.F.)
2 Institute of Intelligent Manufacturing and Precision Machining, Railway Environmental Vibration and Noise Engineer-ing Research Center, East China Jiaotong University, Nanchang 330013, China
3 School of Automotive Studies, Tongji University, Shanghai 201804, China; zhangpeizhi@tongji.edu.cn
4 Department of Mechanical, Energy and Management Engineering (DIMEG), University of Calabria, 87036 Rende, Italy
5 Department of Civil and Environmental Engineering, UCLA, Los Angeles, CA 90095-1405, USA
* Correspondence: letiangao@g.ucla.edu

Abstract: This paper focuses on a comprehensive study of a four-axle vehicle, including dynamics analysis, equivalent modeling methods, and their comparison. Firstly, a linear two-degree lateral dynamic model is established, which has four drive axles and two steer axles. Secondly, the mathematical transfer function expressions for the yaw rate and the centroid sideslip angle were derived on the basis of the model. The steady-state parameters, such as yaw rate gain $G_{\gamma ss}$, centroid sideslip angle gain $G_{\beta ss}$, stability factor K_n, equivalent axial distance l_n, and equivalent centroid sideslip angle coefficient $K_{n'}$ were obtained by using the transfer functions. Then, the steady-state and transient characteristics are roundly discussed, including steady-state parameters, system root trajectory, frequency domain, and time domain. Some recommendations for the four-axle vehicle's parameter design are also given. Finally, for a more simple and efficient analysis of response characteristics of four-axle vehicles and even n ($n > 4$) axle vehicles, the equivalent model is developed for the four-axle vehicle, and comprehensive analyses are presented with four equalization methods, which are based on the inner heart of the approximation triangle, the outer heart of the approximation triangle, the center of gravity of the approximation triangle and the compensation point. Following a thorough analysis of the four, it is determined that the inner approximation triangle solution approach is most suited for four-axle vehicles.

Keywords: four-axle vehicles; dynamic analysis; the steady-state and transient characteristics; equivalent modeling

check for updates

Citation: Zeng, D.; Luo, W.; Yu, Y.; Hu, Y.; Zhang, P.; Carbone, G.; Xie, D.; Fang, H.; Gao, L. Dynamic Analysis and Equivalent Modeling for a Four-Axle Vehicle. *Actuators* **2024**, *13*, 473. https://doi.org/10.3390/act13120473

Academic Editor: Han Sol Kim

Received: 15 October 2024
Revised: 19 November 2024
Accepted: 21 November 2024
Published: 23 November 2024

Copyright: © 2024 by the authors. Licensee MDPI, Basel, Switzerland. This article is an open access article distributed under the terms and conditions of the Creative Commons Attribution (CC BY) license (https://creativecommons.org/licenses/by/4.0/).

1. Introduction

The advancement of vehicle technology has led to an increased need for larger and more substantial vehicles in the fields of transportation engineering and military operations [1–4]. The implementation of a four-axle vehicle has been found to be advantageous in reducing the load exerted on each individual axle, thereby resulting in improved longevity of the vehicle's tires. Additionally, this configuration has been observed to enhance both the maneuverability and stability of the vehicle. However, the elongation of the four-axle vehicle body leads to an increase in overall load and the number of axles, thereby posing challenges to the control of vehicle handling stability. The analysis of response characteristics of four-axle vehicles prior to their configuration is a valuable practice [5,6]. Simultaneously, the research places significant emphasis on the accurate and efficient

equivalent modeling of multi-axle vehicles to facilitate the analysis of their diverse characteristics [7–9].

Numerous scholars and research institutions, both domestically and internationally, have conducted extensive investigations on multi-axle vehicles, leading to a significant array of research outcomes.

In a study conducted by Zhang [10], a method for modeling reconfigurable multi-axis vehicles was proposed. The author established a conceptual framework known as a "Boolean matrix" in order to ascertain various attributes, such as joint configurations, number of axes, and active drive systems. In a comprehensive formulation, it is feasible to integrate multiple-axis and articulated vehicles into a unified system. By employing this approach, the process of modeling the dynamics associated with the addition or removal of axes, joints, or actuators can be accomplished with ease and efficiency. However, the disadvantage is the lack of clear proof of their modeling accuracy.

In their study, Williams et al. [11] formulated a traditional two-axle model and deduced the fundamental principles of equivalent wheelbase and understeer for a three-axle vehicle by directly analyzing the steady-state response of the two-axle model. The findings indicated that the outcomes observed in the steady state scenario were in accordance with the kinematic deductions that disregard the influences of dynamics. In a subsequent study, Williams and colleagues [12] expanded upon the aforementioned concept to encompass vehicles equipped with varying numbers of axles. Additionally, he formulated a comprehensive methodology for investigating the maneuverability of multi-axle vehicles through the utilization of equivalent wheelbase and understeer coefficients. The existing general formulation for the equations that describe the steady-state dynamics of vehicles has been expanded to encompass vehicles with multiple axles. Although their conclusions are supported by a large number of theoretical principles, the shortcoming is that they have not been validated through simulation analysis or experimental research.

In a study conducted by ZhiCheng WU [13], a mathematical model consisting of a two-degree-of-freedom differential equation was developed to describe the motion of a three-axle car with dual-front axle steering. The model incorporated a tire magic formula and was used to perform numerical simulations of the car's steady-state and transient responses to a step input of the steering wheel angle. Additionally, the study investigated the impact of varying the steering angle ratios of the first two axles on the steady-state and transient responses of the car. This analysis was conducted for different axle spacings and positions of the center of mass within these axle spacings. However, it should be pointed out that, although the research results are supported by simulation analysis, the results of this study are only relevant to three-axis vehicles equipped with dual front axle steering, indicating a relatively limited range of applications.

GuangLei Yao et al. [14] developed a two-degree-of-freedom system dynamics model for a multi-axle steering vehicle, specifically focusing on the characteristics of large multi-axle vehicles. By considering a three-axle steering vehicle as a case study, the researchers identified five theoretical steering modes using the zero-center-of-mass lateral deflection proportional control approach. Subsequently, they conducted simulation analyses to examine the steady-state and transient response characteristics of these five steering modes, as well as their respective application ranges. It can be pointed out that their research has theoretical support and simulation analysis. If there is experimental analysis, this article will become even better.

JinQuan Ding [15] formulated a comprehensive set of equations that encompass the essential characteristics of the handling dynamics of a multi-axle vehicle. These equations account for the impact of body roll and multi-axle maneuvering on the overall vehicle dynamics. The equations for a two-degree-of-freedom vehicle, with a mass equivalent to 1 M, were derived by incorporating the effect of side lean into a conventional three-degree-of-freedom vehicle model. This study assesses the steady state characteristics, transient characteristics, and root trajectories of a two-axle vehicle that is exclusively influenced by body roll. It can be pointed out that this study only evaluated the steady-state and transient

characteristics of dual-axis vehicles affected only by body roll. If these characteristics of the vehicle could be evaluated from multiple angles, it would be even better.

The mathematical model of a six-axle vehicle with four-axle steering was developed by Waqar Ahmed [16]. Simulations were conducted to enhance the vehicle's steering parameters and maneuverability by varying the track radii, vehicle speeds, and steering ratios pertaining to the first, second, fifth, and sixth steering axles. The evaluation encompassed the analysis of the axle steering angle, wheel side deflection angle, and steering ratio in relation to variations in vehicle speed and turning radius. The implementation of modifications resulted in enhanced performance of the vehicle in terms of its maneuverability and cornering characteristics, as observed with the adoption of the newly chosen configuration.

In their study, ShuFeng Wang [17] conducted an analysis of the multi-axis dynamic steering technology and examined the steering angle control strategy with the aim of enhancing the agility and handling stability of a three-axis vehicle across various speeds. The steering angle ratios in various steering modes are derived by constructing a two-degree-of-freedom model, utilizing the center-of-mass zero side-slip angle, and implementing a proportional control strategy. The simulation and comparison of the steering performance of a three-axle vehicle in three distinct steering modes, namely six-wheel steering, four-wheel steering, and two-wheel steering, are conducted. The empirical findings demonstrate that the implementation of a multi-axle power steering system in a vehicle yields significant enhancements in low-speed maneuverability and high-speed stability. However, it can be pointed out that these articles would be even better if they could have experimental analysis.

This paper presents an analysis of a four-axis vehicle using a linear two-degree-of-freedom model. The study includes the derivation of conventional parameters, such as the steady state of yaw rate, the steady state of centroid sideslip angle, the stability factor, and equivalent axle spacing. Additionally, this research introduces parameters that are rarely discussed, namely the steering center distance and the transient steering center distance. The simulation and analysis of the steady-state characteristics, stability, and transient characteristics were conducted. The relationship between steady-state parameters and various factors, such as vehicle speed, stability factor, tire sideslip stiffness, and steering center distance is determined. Additionally, recommendations for the parameter design of a four-axle vehicle are provided. Furthermore, to enhance the ease and efficiency of analyzing multi-axle vehicles, alternative approaches, such as the inner heart method, outer heart method, and compensation point method, based on the approximate triangle concept, have been suggested and simulated for the purpose of comparison and analysis.

2. Dynamic Modeling for Four-Axis Vehicles

2.1. Model Description

To enhance the convenience of studying the response characteristics of the four-axis vehicle, this research paper simplifies the four-axis vehicle by considering a model with only two degrees of freedom [18,19], namely lateral motion and yaw motion. The following assumptions are made:

(1) Assuming a constant longitudinal vehicle speed and neglecting the influence of air resistance;

(2) The tire's lateral deflection characteristics exhibit linearity, meaning that the lateral force exerted by the tire is directly proportional to the angle of lateral deflection. Additionally, the tire's lateral deflection stiffness remains constant;

(3) It is postulated that the left and right tires possess identical characteristics, and the influence of load transfer is disregarded;

(4) In the steering angle input study, it is assumed that the steering angle is not large and is directly input by each axis;

(5) The impact of body roll characteristics on steering performance is disregarded.

Based on the above assumptions, the four-axis vehicle in this paper can be simplified to a linear two-degree-of-freedom model as shown in Figure 1. The following definitions are

made for this two-degree-of-freedom model: Firstly, numbers ①, ②, ③, and ④ respectively represent the position and status of the first, second, third, and fourth axle wheels. Secondly, the center of mass of the vehicle is at point O, the x-axis represents the direction of the vehicle's forward movement, the y-axis represents the left side of the vehicle's forward direction, and the z-axis represents the upward direction perpendicular to the ground. Next, the longitudinal speed u at the center of mass of the vehicle is in the same direction as the x-axis in the vehicle coordinate system, the lateral speed v is in the same direction as the y-axis, the yaw rate γ of the vehicle rotates counterclockwise around the z-axis, and the vehicle's centroid sideslip angle is β. Then, l_1 is the displacement from the first axis of the vehicle to the center of mass position O, l_2 is the displacement from the second axis of the vehicle to the center of mass position O, l_3 is the displacement from the third axis of the vehicle to the center of mass position O, and l_4 is the displacement from the fourth axis of the vehicle to the center of mass position O. Then, δ_1 and δ_2 are the sideslip angles of the first and second axes, respectively. Next, v_1, v_2, v_3, and v_4 are the velocities at the midpoints of the first, second, third, and fourth axes, respectively. Then, α_1, α_2, α_3, and α_4 are the sideslip angles of the first, second, third, and fourth axes, respectively. Next, F_{yw1}, F_{yw2}, F_{yw3}, and F_{yw4} represent the tire lateral forces acting on the first, second, third, and fourth axles, respectively. Finally, the turning center of the vehicle is the O_R point, the projection point of the rotation center on the x-axis is the O_H point, and the displacement from the center of mass position O to the O_H point is l_R, which is the distance between the turning centers. However, when a vehicle is turning at a certain speed, it requires the centripetal force of the ground to provide power for it to make a certain circular motion. Therefore, each tire will produce a corresponding side slip angle to provide it with the required lateral force, so the vehicle's turning center will move forward at this time. The $O_{R'}$ point is the instantaneous turning center of the vehicle, while $l_{R'}$ is the instantaneous turning center distance.

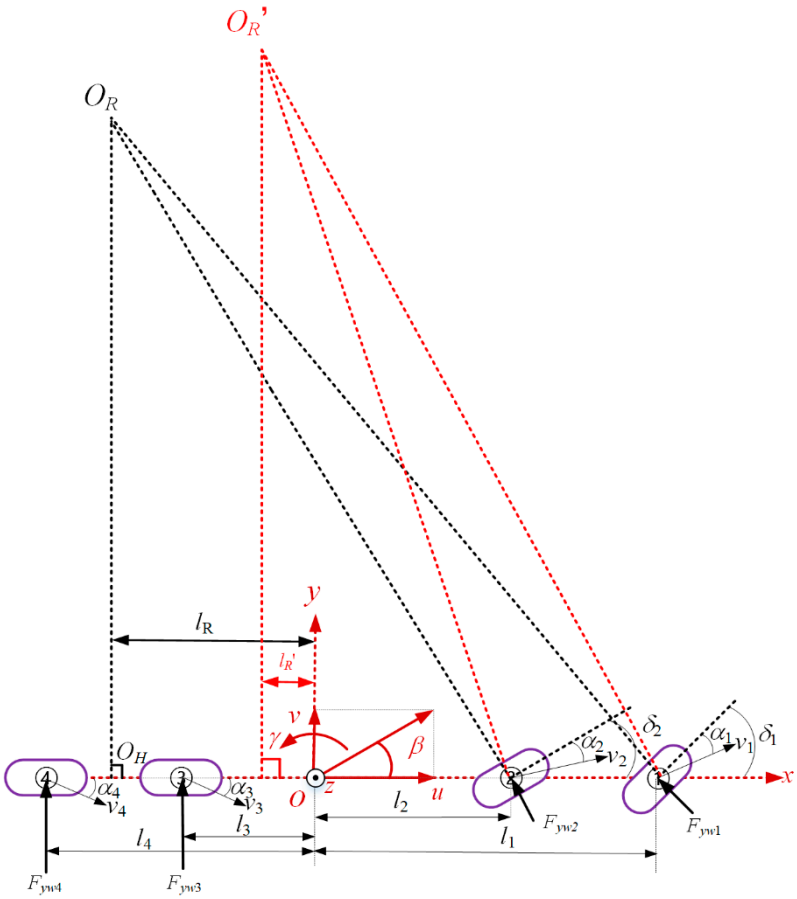


Figure 1. Linear two-degree-of-freedom model of a four-axis vehicle.

In order to facilitate future research on repeatability and sustainability by scholars, the vehicle parameters used in this article are presented in Table 1.

Table 1. Vehicle parameters.

Symbol	Parameter	Reference Value	Symbol	Parameter	Reference Value
$\boldsymbol{m}$	vehicle mass	12,200 (kg)	l_4	Displacement of fourth axle to the center of mass position	−2.2 (m)
$\boldsymbol{I_{zz}}$	vehicle inertia around the z-axis	60,000 (kg × m^2)	K_1	First axle wheel tire sideslip stiffness	200,000
$\boldsymbol{l_1}$	the displacement of first axle to the center of mass position	1.8 (m)	K_2	Second axle wheel tire sideslip stiffness	200,000
$\boldsymbol{l_2}$	the displacement of second axle to the center of mass position	0.5 (m)	K_3	Third axle wheel tire sideslip stiffness	200,000
$\boldsymbol{l_3}$	the displacement of third axle to the center of mass position	−0.85 (m)	K_4	Fourth axle wheel tire sideslip stiffness	200,000

2.2. Dynamic Model Derivation

In Figure 1, only the lateral motion and yaw motion of the vehicle are considered, without considering the influence of longitudinal forces. According to Newton's second law, the equilibrium equation for the lateral motion of the vehicle can be obtained as Equation (1):

$$m * (\dot{v} + \gamma u) = F_{yw1}\cos\delta_1 + F_{yw2}\cos\delta_2 + F_{yw3} + F_{yw4} \quad (1)$$

where m represents the overall mass of the vehicle; v represents the lateral speed of the vehicle; γ represents the yaw rate of the vehicle; u represents the longitudinal speed of the vehicle; δ_1 and δ_2 are the sideslip angles of the first and second axes, respectively; F_{yw1}, F_{yw2}, F_{yw3}, and F_{yw4} represent the tire lateral forces acting on the first, second, third, and fourth axles, respectively.

In Figure 1, because the direction of the yaw rate γ rotates counterclockwise around the z-axis, its yaw toque also rotates counterclockwise around the z-axis. Based on the combined torque of the tire forces in the counterclockwise direction, the vehicle's yaw balance equation can be obtained as Equation (2):

$$I_{zz} * \dot{\gamma} = F_{yw1}\cos\delta_1 l_1 + F_{yw2}\cos\delta_2 l_2 + F_{yw3} l_3 + F_{yw4} l_4 \quad (2)$$

where I_{zz} is the vehicle inertia around the z-axis; l_1 is the displacement from the first axis of the vehicle to the center of mass position O; l_2 is the displacement from the second axis of the vehicle to the center of mass position O; l_3 is the displacement from the third axis of the vehicle to the center of mass position O; and l_4 is the displacement from the fourth axis of the vehicle to the center of mass position O.

When the steering angle δ_1 and δ_2 is not large, $cos\ \delta_1 \approx 1$, $cos\ \delta_2 \approx 1$. So, Equations (1) and (2) can be simplified to Equations (3) and (4):

$$m * (\dot{v} + \gamma u) = \sum_{i=1}^{4} F_{ywi} \quad (3)$$

$$I_{zz} * \dot{\gamma} = \sum_{i=1}^{4} (F_{ywi} l_i) \quad (4)$$

In the vehicle coordinate system, the centroid sideslip angle β is usually defined as the angle between the velocity direction of the center of mass and the forward direction of the vehicle. The vehicle's centroid sideslip angle $\beta = \frac{v}{u}$; because the longitudinal speed u remains constant, we have $\dot{\beta} = \frac{\dot{v}}{u}$, thus obtaining Equations (5) and (6):

$$\dot{\beta} = \frac{\sum_{i=1}^{4} F_{ywi}}{mu} - \gamma \tag{5}$$

$$\dot{\gamma} = \frac{\sum_{i=1}^{4} \left(F_{ywi} l_i\right)}{I_{zz}} \tag{6}$$

Under the assumption that the tire characteristics are in the linear region, the tire the sideslip force is proportional to the sideslip angle, thus obtaining Equation (7):

$$F_{ywi} = K_i \alpha_i \tag{7}$$

where K_i is the sideslip stiffness of the ith (i = 1, 2, 3, 4) axis of the vehicle, and α_i are the sideslip angles of the ith (i = 1, 2, 3, 4) axis of the vehicle.

According to the coordinate system and geometric relationship regulations, if the tire sideslip angle is defined as positive in the counterclockwise direction of the x-axis, Equation (8) can be obtained:

$$\alpha_i = \delta_i - \left(\beta + \frac{l_i \gamma}{u}\right) \tag{8}$$

Substituting Equations (7) and (8) into Equations (5) and (6) yields the state space equations for the linear two-degree-of-freedom model of the four-axis vehicle:

$$\begin{bmatrix} \dot{\beta} \\ \dot{\gamma} \end{bmatrix} = \begin{bmatrix} -\frac{\sum_1^4 K_i}{mu} & -1 - \frac{\sum_1^4 (K_i l_i)}{mu^2} \\ -\frac{\sum_1^4 (K_i l_i)}{I_{zz}} & -\frac{\sum_1^4 \left(K_i {l_i}^2\right)}{I_{zz} u} \end{bmatrix} \begin{bmatrix} \beta \\ \gamma \end{bmatrix} + \begin{bmatrix} \frac{K_1}{mu} & \frac{K_2}{mu} \\ \frac{K_1 l_1}{I_{zz}} & \frac{K_2 l_2}{I_{zz}} \end{bmatrix} \begin{bmatrix} \delta_1 \\ \delta_2 \end{bmatrix} \tag{9}$$

In Figure 2, based on the Ackermann turning geometry model [20,21], a turning kinematic modeling of the monorail model is established, and Equations (10) and (11) can be obtained from the geometric relationships:

$$\tan \delta_1 = \frac{l_{13} + \frac{1}{2} l_{34}}{R} \tag{10}$$

$$\tan \delta_2 = \frac{l_{23} + \frac{1}{2} l_{34}}{R} \tag{11}$$

where l_{13} is the distance from the first axis of the vehicle to the third axis, $l_{34} = l_3 - l_4$; l_{34} is the distance from the third axis of the vehicle to the fourth axis, $l_{34} = l_3 - l_4$; and l_{23} is the distance from the second axis of the vehicle to the third axis, $l_{23} = l_2 - l_3$.

The relationship between δ_1 and δ_2 can be obtained from Equations (10) and (11):

$$\delta_2 = \frac{2l_{23} + l_{34}}{2l_{13} + l_{34}} \delta_1 = \frac{2l_2 - l_3 - l_4}{2l_1 - l_3 - l_4} \delta_1 = N \delta_1 \tag{12}$$

where N represents a constant about l_1, l_2, l_3, and l_4.

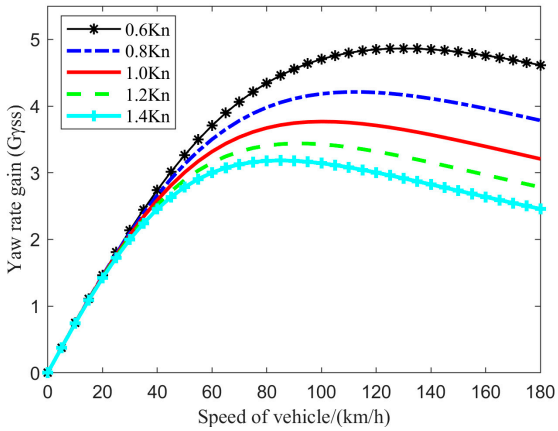


Figure 2. Vehicle Yaw Rate Gain versus Vehicle Speed Curve.

By substituting Equation (12) into Equation (9), the final state space equation of the linear two degrees of freedom model for a four-axle vehicle can be obtained as Equation (13):

$$\begin{bmatrix} \dot{\beta} \\ \dot{\gamma} \end{bmatrix} = \begin{bmatrix} -\frac{\sum_1^4 K_i}{mu} & -1-\frac{\sum_1^4 (K_i l_i)}{mu^2} \\ -\frac{\sum_1^4 (K_i l_i)}{I_{zz}} & -\frac{\sum_1^4 \left(K_i {l_i}^2\right)}{I_{zz} u} \end{bmatrix} \begin{bmatrix} \beta \\ \gamma \end{bmatrix} + \begin{bmatrix} \frac{K_1 + NK_2}{mu} \\ \frac{K_1 l_1 + NK_2 l_2}{I_{zz}} \end{bmatrix} [\delta_1] \tag{13}$$

3. Steady-State Characteristics Analysis

3.1. Steady-State Model Derivation

Using the centroid sideslip angle β and yaw rate γ as state variables, Laplace transforms the state space Equation (13) of the linear two degrees of freedom model of a four-axle vehicle to obtain Equations (14) and (15):

$$\left(s + \frac{\sum_1^4 K_i}{mu}\right)\beta(s) + \left[1 + \frac{\sum_1^4 (K_i l_i)}{mu^2}\right]\gamma(s) = \frac{K_1 + NK_2}{mu}\delta_1(s) \tag{14}$$

$$\frac{\sum_1^4 (K_i l_i)}{I_{zz}}\beta(s) + \left[s + \frac{\sum_1^4 \left(K_i {l_i}^2\right)}{I_{zz} u}\right]\gamma(s) = \frac{K_1 l_1 + NK_2 l_2}{I_{zz}}\delta_1(s) \tag{15}$$

where s represents the Laplace variable.

Equations (14) and (15) are linked and eliminated to obtain the transfer function of the centroid sideslip angle β and the yaw rate γ on the steering angle δ_1:

$$\frac{\beta(s)}{\delta_1(s)} = \frac{\frac{K_1+NK_2}{mu}s + \frac{(K_1+NK_2)\cdot\sum_1^4\left(K_i {l_i}^2\right) - mu^2(K_1 l_1+NK_2 l_2) - (K_1 l_1+NK_2 l_2)\sum_1^4 (K_i l_i)}{I_{zz} mu^2}}{s^2 + \frac{I_{zz}\sum_1^4 K_i + m\sum_1^4\left(K_i {l_i}^2\right)}{I_{zz} mu}s + \frac{\sum_1^4 K_i \cdot \sum_1^4\left(K_i {l_i}^2\right) - \left[\sum_1^4 (K_i l_i)\right]^2 - mu^2\sum_1^4 (K_i l_i)}{I_{zz} mu^2}} \tag{16}$$

$$\frac{\gamma(s)}{\delta_1(s)} = \frac{\frac{K_1 l_1+NK_2 l_2}{I_{zz}}s + \frac{(K_1 l_1+NK_2 l_2)\sum_1^4 K_i - (K_1+NK_2)\sum_1^4 (K_i l_i)}{I_{zz} mu}}{s^2 + \frac{I_{zz}\sum_1^4 K_i + m\sum_1^4\left(K_i {l_i}^2\right)}{I_{zz} mu}s + \frac{\sum_1^4 K_i \cdot \sum_1^4\left(K_i {l_i}^2\right) - \left[\sum_1^4 (K_i l_i)\right]^2 - mu^2\sum_1^4 (K_i l_i)}{I_{zz} mu^2}} \tag{17}$$

The steady-state characteristic of a system is the output characteristic of the system when the time tends to be infinite under the action of a typical signal [22]. At a steady state, the rate of change in the state quantities is 0. Let the Laplace variables of the yaw rate transfer function $\gamma(s)/\delta_1(s)$ and the centroid sideslip angle transfer function $\beta(s)/\delta_1(s)$ be

$s = 0$ to obtain the steady-state gains of the yaw rate and the centroid sideslip angle for the steering angle δ_1 as $G_{\gamma ss}$ and $G_{\beta ss}$, respectively:

$$G_{\gamma ss} = \frac{\gamma_{ss}}{\delta_{1ss}} = \frac{u}{l_n(1 + u^2 K_n)} \tag{18}$$

$$G_{\beta ss} = \frac{\beta_{ss}}{\delta_{1ss}} = \frac{l_n{}' + k_n{}' u^2}{l_n(1 + u^2 K_n)} \tag{19}$$

where l_n is the equivalent wheelbase of the four-axle vehicle, K_n is the stability factor of the four-axle vehicle, and K_n is an important parameter characterizing the steady state response of the vehicle. When $K_n < 0$, the vehicle exhibits oversteer; when $K_n = 0$, the vehicle exhibits neutral steering; when $K_n > 0$, the vehicle exhibits understeer. While ln′ is the equivalent steering center distance of the four-axle vehicle, $K_{n'}$ is defined as the equivalent centroid sideslip angle coefficient of the four-axle vehicle. The following are the expressions for these parameters:

$$l_n = \frac{\sum_1^4 K_i \cdot \sum_1^4 \left(K_i {l_i}^2\right) - \left[\sum_1^4 (K_i l_i)\right]^2}{K_1 \sum_1^4 [K_i (l_1 - l_i)] + N K_2 \sum_1^4 [K_i (l_2 - l_i)]} \tag{20}$$

$$K_n = \frac{-m \sum_1^4 (K_i l_i)}{\sum_1^4 K_i \cdot \sum_1^4 \left(K_i {l_i}^2\right) - \left[\sum_1^4 (K_i l_i)\right]^2} \tag{21}$$

$$l_n{}' = -\frac{K_1 \sum_1^4 [K_i l_i (l_1 - l_i)] + N K_2 \sum_1^4 [K_i l_i (l_2 - l_i)]}{K_1 \sum_1^4 [K_i (l_1 - l_i)] + N K_2 \sum_1^4 [K_i (l_2 - l_i)]} \tag{22}$$

$$K_n{}' = -\frac{m(K_1 l_1 + N K_2 l_2)}{K_1 \sum_1^4 [K_i (l_1 - l_i)] + N K_2 \sum_1^4 [K_i (l_2 - l_i)]} \tag{23}$$

In a steady state, the instantaneous steering radius R' of the vehicle can be expressed as the following expression:

$$R' = \frac{u}{\gamma_{ss}} \tag{24}$$

where R' represents the instantaneous turning radius of the vehicle and γ_{ss} represents the steady-state yaw rate of the vehicle.

When the first axis steering angle is not large, the instantaneous steering radius R' of the vehicle can also be expressed as the following:

$$l_R{}' + l_1 = R' \tan(\delta_1 - \alpha_1) = R'(\delta_1 - \alpha_1) = R'\left(\beta_{ss} + \frac{l_1 \gamma_{ss}}{u}\right) \tag{25}$$

where $l_{R'}$ is the instantaneous turning center distance and β_{ss} is the steady-state centroid sideslip angle of the vehicle.

From (24) and (25), the instantaneous steering center distance $l_{R'}$ of the vehicle can be obtained as follows:

$$l_R{}' = \frac{\beta_{ss}}{\gamma_{ss}} u = l_n{}' + k_n{}' u^2 \tag{26}$$

The ratio of the steering radius of a vehicle is the ratio of the instantaneous steering radius to the steering radius, and they also have the following relationship:

$$\frac{R'}{R} = 1 + u^2 K_n \tag{27}$$

where R represents the turning radius.

When the first axis steering angle is not large, the steering radius R of the vehicle can also be expressed as follows:

$$l_R + l_1 = R\tan\delta_1 = R\delta_1 \tag{28}$$

where l_R is steering center distance.

With (18), (24) and (27), the vehicle steering center distance l_R can be obtained as follows:

$$l_R = \frac{R'\delta_{1ss}}{1+u^2K_n} = \frac{u\delta_{1ss}}{(1+u^2K_n)\gamma_{ss}} = \frac{u}{(1+u^2K_n)G_{\gamma ss}} = l_n - l_1 \tag{29}$$

3.2. Steady-State Characteristics

After deriving the steady-state parameters related to the vehicle, the trend of the steady-state characteristics of the vehicle system under different input conditions can be analyzed and studied. Firstly, analyze the steady-state gain of the vehicle's yaw rate, which refers to the ratio of steady-state yaw rate to front wheel steering angle, which is also known as steering sensitivity and is a key parameter that affects the stability of the vehicle system.

As shown in Figure 2, it can be seen from the data in the figure that within the speed range of 0–50 km/h, the yaw rate gain shows a linear increase trend with longitudinal vehicle speed, and is basically not affected by the stability factor K_n. In the speed range of 50–100 km/h, the yaw rate gain increases with the increase in longitudinal vehicle speed, and the growth rate slows down significantly and is greatly affected by the stability factor K_n. Subsequently, as the vehicle speed continues to increase, after reaching a certain critical speed, the yaw rate gain will reach its peak, and the maximum yaw rate gain corresponding to the vehicle speed is called the characteristic vehicle speed. Subsequently, as the vehicle speed continues to increase, the gain of the car's yaw rate will show a decreasing trend.

Therefore, according to the image data, the stability factor K_n of the four-axle electric wheel drive vehicle in this article is greater than 0, indicating that the vehicle has the characteristic of insufficient steering. Meanwhile, as mentioned above, under low-speed driving conditions, the stability factor K_n has a relatively small impact on the gain of the vehicle's yaw rate and can be ignored. However, as the vehicle speed increases, the influence of the stability factor K_n on the yaw rate gain becomes increasingly apparent: a larger stability factor K_n will make the vehicle more stable at high speeds.

Secondly, the relationship between the ratio of vehicle steering radius and vehicle speed and stability factors is analyzed. As shown in Equation (26), the ratio of the steering radius of the vehicle is the ratio of the instantaneous steering radius of the vehicle to the steering radius, and the size of its value is related to the vehicle speed u and the stability factor K_n. As shown in Figure 3, with the increase in vehicle speed, the ratio of the steering radius of the vehicle from the origin 1 non-linearly increases, and the slope is also increasing. This shows that the instantaneous steering center of the vehicle is shifted forward as the speed increases. It also shows that the stability factor K_n of the vehicle is greater than 0, i.e., the vehicle has understeer characteristics, and this result is consistent with the conclusions analyzed in Figure 2.

Next, analyze the gain of the vehicle's centroid sideslip angle. As shown in Figure 4, it can be seen from the figure that at low speeds, i.e., within the speed range of 0–50 km/h, the gain of the vehicle's centroid sideslip angle will change from positive to zero and then to negative, and is basically not affected by the stability factor K_n. Subsequently, as the vehicle speed continues to increase, the gain of the centroid sideslip angle will continue to increase negatively and will be increasingly influenced by the stability factor K_n.

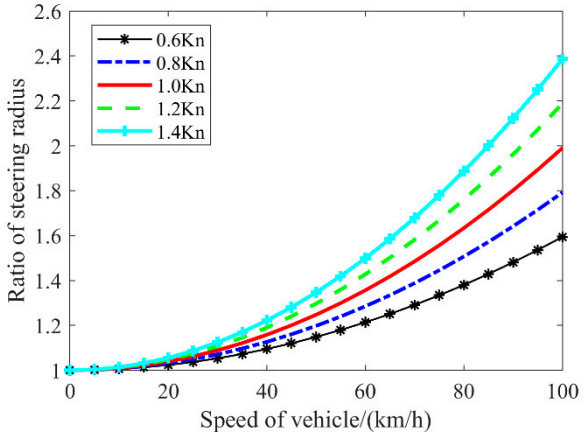


Figure 3. Vehicle steering radius ratio and speed curve.

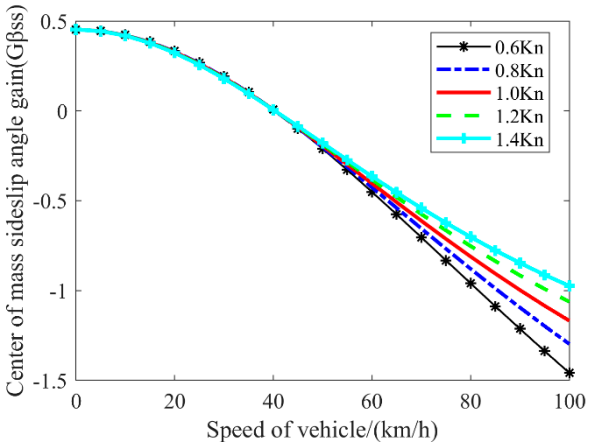


Figure 4. Vehicle's centroid sideslip angle gain versus vehicle speed curve.

Therefore, it can be concluded that during high-speed driving, a significant stability factor K_n can reduce the gain of the centroid sideslip angle, which will help to improve the stability of the vehicle's sideslip. However, for every 0.2 times increase in K_n, the amplitude of the corresponding decrease in the gain of the centroid sideslip angle will decrease. Therefore, the method of ensuring the high-speed driving stability of the vehicle by increasing the stability factor K_n is limited.

From the previous analysis, it can be seen that the stability factor K_n has a significant impact on the stability of the vehicle system during high-speed driving. So next, it is necessary to fully understand which parameters of the vehicle affect the stability factor K_n.

In Equation (21), the tire sideslip stiffness of the four axes is K_i (i = 1, 2, 3, 4). In order to better analyze and study, this paper sets them all to the same tire sideslip stiffness K_y, which can be simplified into Equation (30). In Equation (30), the stability coefficient K_n is mainly influenced by parameters, such as the total mass m of the vehicle, the displacement l_i from the axle to the center of mass of the vehicle, and the sideslip stiffness K_y of the vehicle tires. However, generally speaking, it is difficult to adjust parameters, such as the total mass m of the vehicle and the displacement l_i from the axle to the vehicle center of mass, and only the tire sideslip stiffness K_y of the vehicle is relatively easy to adjust. Therefore, the next focus is to analyze the influence of the stability coefficient K_n on the tire sideslip stiffness K_y.

$$K_n = \frac{-m\sum_1^4 (K_y l_i)}{4K_y \cdot \sum_1^4 \left(K_y {l_i}^2\right) - \left[\sum_1^4 (K_y l_i)\right]^2} \tag{30}$$

Figure 5 shows the relationship between stability factor K_n and tire sideslip angle K_y. It can be seen from the figure that within the range of tire sideslip stiffness 200,000~400,000, the stability factor K_n will gradually decrease with the increase in tire sideslip stiffness K_y, which is unfavorable for the stability of the vehicle during high-speed driving. Therefore, in order to increase the stability factor K_n and ensure the stability of the vehicle during high-speed driving, the tire sideslip stiffness K_y of the vehicle should be adjusted to be lower.

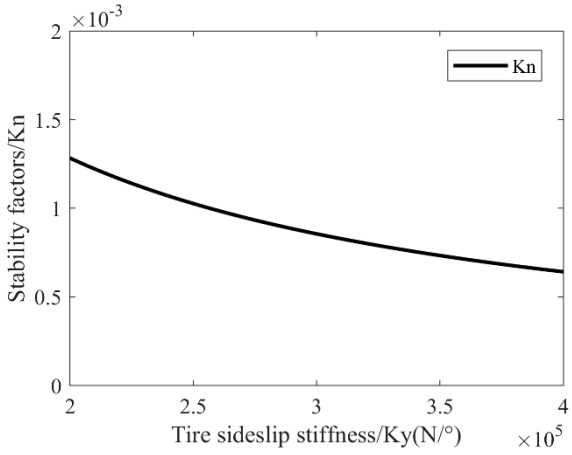


Figure 5. Variation curves of K_n with tire sideslip stiffness K_y.

As shown in Figure 6, the variation curves of the yaw rate gain with the tire sideslip stiffness at different vehicle speeds are shown. It can be seen that at the same vehicle speed, as the tire sideslip stiffness increases, the trend of the yaw rate gain also increases, but the magnitude of their increase is different. At the same tire sideslip stiffness, the yaw rate gain also increases with the increase in vehicle speed. A detailed comparison shows that the magnitude of the yaw rate gain with the increase in tire sideslip angle is different for different speeds. At a low speed of 20 km/h, the magnitude of the yaw rate gain with the tire sideslip angle is particularly small, and the effect is almost negligible; while at a high speed of 100 km/h, the yaw rate gain with the tire sideslip has a more obvious tendency to increase, and thus there is a possibility of influencing the stability of the vehicle's handling. Therefore, when the vehicle is running at high speed, the tire sideslip stiffness is appropriately low for better pendulum stability. The results of this analysis are consistent with those in Figure 5.

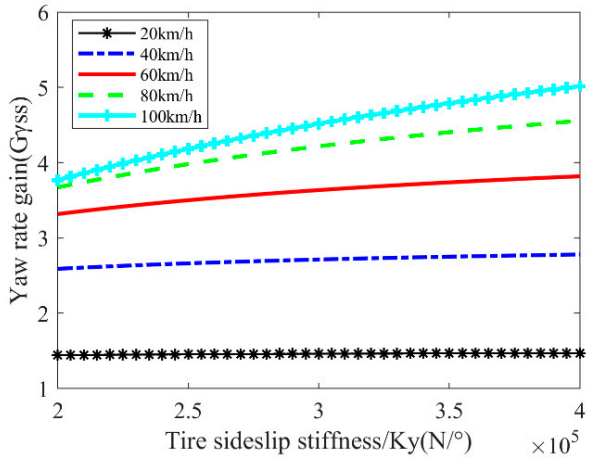


Figure 6. Variation curves of yaw rate gain with tire sideslip stiffness at different vehicle speeds.

As shown in Figure 7, the variation curves of the centroid sideslip angle gain with the tire sideslip stiffness at different vehicle speeds are shown. At the same vehicle speed,

the centroid sideslip angle gain increases with the increase in tire sideslip stiffness; at the same tire sideslip stiffness, the centroid sideslip angle gain decreases with the increase in vehicle speed. In general, we would like to keep the control strategy with zero centroid sideslip angle; therefore, at low speeds, it is better to keep the tire sideslip stiffness low. At medium and high speeds, the tire sideslip stiffness should be higher because it can keep the centroid sideslip angle as low as possible, which is helpful for the vehicle's side deflection stability.

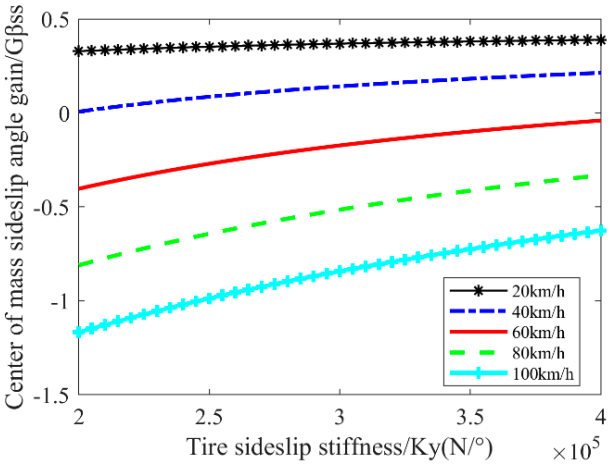


Figure 7. Variation curves of centroid sideslip angle gain with tire sideslip stiffness at different vehicle speeds.

However, the results of this figure at high vehicle speeds contradict the results of the analyses in Figure 6. Therefore, it is necessary to compare the degree of influence of high and low tire sideslip stiffness on the vehicle sway stability and lateral stability at 100 km/h vehicle speed. By comparing Figures 7 and 8, it can be seen that the benefits of low tire sideslip stiffness to the vehicle's sway stability are more obvious than the drawbacks to the vehicle's sideslip stability. In conclusion, at high speeds, a lower tire sideslip stiffness is more beneficial to the overall stability of the vehicle.

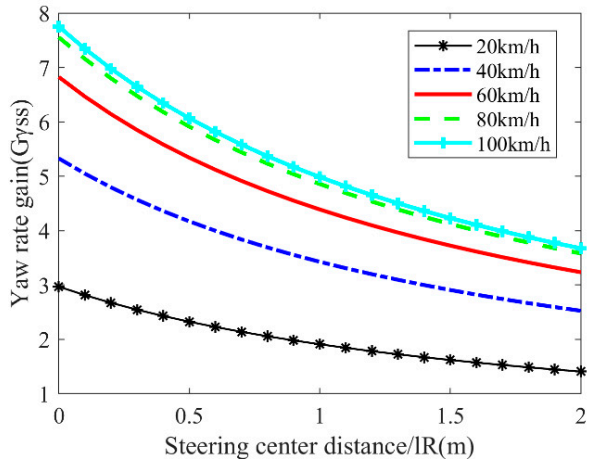


Figure 8. Variation curves of yaw rate gain with steering center distance at different vehicle speeds.

In order to analyze the influence of the steering center distance l_R on the vehicle, the tire sideslip stiffness K_y is set to 200,000. As shown in Figure 8, it can be seen from the figure that at a speed of 20 km/h, the starting point of the yaw rate gain is around 3, and it decreases with the increase in the steering center distance l_R. At a speed of 40 km/h, the starting point of the yaw rate gain is around 5.3, and it decreases with the increase in the steering center distance l_R. At a speed of 60 km/h, the starting point of the yaw rate gain is

around 6.8, and it decreases with the increase in the steering center distance l_R. Similarly, at speeds of 80 km/h and 100 km/h, the yaw rate gain also decreases as the steering center distance l_R increases.

Therefore, it can be concluded that the yaw rate gain will decrease with the increase in the steering center distance l_R, and the starting point of the yaw rate gain will be larger as the vehicle speed increases. In order to improve the yaw stability of the vehicle, it is better to have a larger steering center distance.

As shown in Figure 9, it can be seen from the figure that at a speed of 20 km/h, the starting point of the absolute value of the centroid sideslip angle gain is around 0.7, which decreases with the increase in the steering center distance and is closer to zero centroid sideslip angle; At a speed of 40 km/h, the starting point of the absolute value of the centroid sideslip angle gain is around 0, and it will slowly approach zero centroid sideslip angle as the steering center distance increases. At a speed of 60 km/h, the starting point of the absolute value of the centroid sideslip angle gain is around 0.8, which decreases as the steering center distance increases and gradually approaches zero centroid sideslip angle. Similarly, at speeds of 80 km/h and 100 km/h, the absolute value of the centroid sideslip angle will also decrease as the steering center distance increases, getting closer to zero centroid sideslip angle.

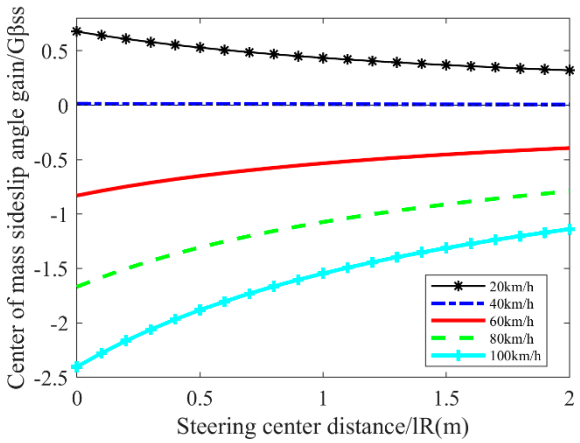


Figure 9. Variation curves of centroid sideslip angle gain with steering center distance at different vehicle speeds.

We conclude that increasing the steering center distance of the vehicle will bring the gain of the centroid sideslip angle closer to zero. Therefore, in order to ensure the principle of zero centroid sideslip angle as much as possible, increasing the steering center distance of the vehicle will be more conducive to stable driving.

3.3. Summary and Suggestions

After analyzing the steady-state characteristics of the vehicle in Section 3.2, the following can be concluded: 1. When the vehicle is running at medium and high speeds, the stability factor K_n has a significant impact on the stability of the vehicle. Reasonably increasing the stability factor K_n of the vehicle is beneficial for improving its driving stability. 2. A smaller vehicle tire sideslip stiffness K_y can improve the stability factor K_n of the vehicle and reduce the yaw rate gain during high-speed driving, thereby improving the stability of vehicle operation. 3. Reasonably increasing the steering center distance can reduce the absolute values of the vehicle's yaw rate gain and centroid sideslip angle gain, thereby improving the stability of vehicle operation. Therefore, for manufacturers of four-axle vehicles, increasing the stability factor K_n reasonably, reducing tire sideslip stiffness K_y reasonably, and increasing the steering center distance reasonably will be beneficial for the stability and safety of four-axle vehicles operating under extreme conditions.

4. Transient Characteristics Analysis

4.1. Transient Model Derivation

Equations (16) and (17) are the transfer functions of the centroid sideslip angle β and the yaw rate γ on the steering angle δ_1 of a four-axle vehicle, which are now organized into the form of standard transfer functions:

$$G_{\beta(s)} = \frac{\beta(s)}{\delta_1(s)} = G_{\beta ss}\frac{T_\beta s + 1}{T_2 s^2 + T_1 s + 1} \tag{31}$$

$$G_{\gamma(s)} = \frac{\gamma(s)}{\delta_1(s)} = G_{\gamma ss}\frac{T_\gamma s + 1}{T_2 s^2 + T_1 s + 1} \tag{32}$$

The expressions for the coefficients T_β, T_γ, T_1, and T_2 of Equations (31) and (32) are as follows, respectively:

$$T_\beta = \frac{I_{zz}u(K_1 + NK_2)}{(K_1 + NK_2)\sum_1^4\left(K_i {l_i}^2\right) - mu^2(K_1 l_1 + NK_2 l_2) - (K_1 l_1 + NK_2 l_2)\sum_1^4(K_i l_i)} \tag{33}$$

$$T_\gamma = \frac{mu(K_1 l_1 + NK_2 l_2)}{K_1\sum_1^4\left[K_i(l_1 - l_i)\right] + NK_2\sum_1^4[K_i(l_2 - l_i)]} \tag{34}$$

$$T_1 = \frac{u\left[I_{zz}\sum_1^4 K_i + m\sum_1^4\left(K_i {l_i}^2\right)\right]}{\sum_1^4 K_i \cdot \sum_1^4\left(K_i {l_i}^2\right) - \left[\sum_1^4(K_i l_i)\right]^2 - mu^2\sum_1^4(K_i l_i)} \tag{35}$$

$$T_2 = \frac{I_{zz}mu^2}{\sum_1^4 K_i \cdot \sum_1^4\left(K_i {l_i}^2\right) - \left[\sum_1^4(K_i l_i)\right]^2 - mu^2\sum_1^4(K_i l_i)} \tag{36}$$

4.2. System Root Trajectory Analysis

From the transfer Functions (31) and (32), the characteristic equation of the system is as follows:

$$T_2 s^2 + T_1 s + 1 = 0 \tag{37}$$

T_2 and T_1 are known, so the system stability of the four-axle vehicle can be judged by the situation of the characteristic roots of the characteristic equations:

① If the characteristic roots are all negative real roots or conjugate complex roots with negative real parts, the system is stable;

② If at least one of the characteristic roots contains a positive real part, the system is unstable;

③ If the characteristic roots contain imaginary roots and the other characteristic roots have negative real parts, the system is critically stable.

Since the characteristic roots of the mathematical solution of Equation (37) are more complicated, the stability of the system is analyzed in this section using the method of root trajectory graphing [23]. The root trajectory method is based on the known open-loop poles and zero distribution of each given feedback system, through the change in system parameters to solve the characteristic equations, that is, according to the parameter changes in the study of the system closed-loop poles distribution of a graphical method. For the four-axle vehicle studied in this paper, the change in this system parameter is the change in vehicle speed (10~100 m/s, one point per 10 m/s interval).

As shown in Figure 10, which shows the root trajectory of the system, it can be seen that all the characteristic roots of the system are negative real roots as well as conjugate complex roots with negative real parts, so it means that the system has been in a stable state. Also, it can be seen that the characteristic roots are getting closer and closer to the imaginary axis as the vehicle speed increases. This indicates that the stability of the system is deteriorating as the vehicle speed increases.

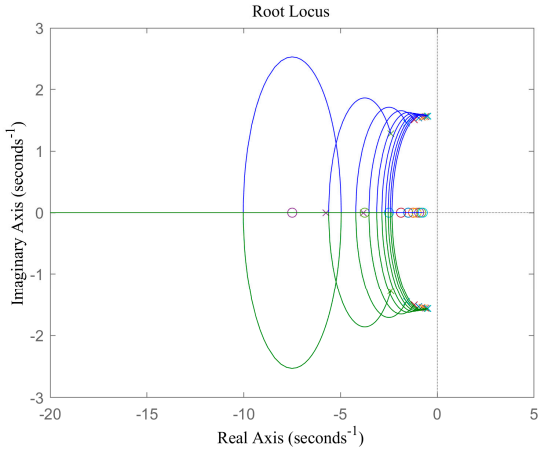


Figure 10. System root trajectory diagram.

4.3. Frequency Domain Analysis

In order to further analyze the response characteristics of four-axle vehicles at different input frequencies, based on the transfer Function (32), the frequency domain characteristics of the yaw rate are analyzed using Bode plots.

As shown in Figure 11, the frequency domain characteristic curves of the vehicle's yaw rate at different vehicle speeds are presented. The upper part is the amplitude-frequency characteristic, and the lower part is the phase frequency characteristic. From the graph, it can be seen that, within the frequency range of 10^{-1} to 10^{0}, the amplitude is the smallest at a speed of 20 km/h, followed by 40 km/h, 60 km/h, and 80 km/h. The maximum amplitude is 100 km/h, and the amplitude increases with the increase in vehicle speed. In the frequency range of 10^{0}–10^{1}, as the input frequency increases, the amplitude first remains stable and then gradually decreases. In the frequency range of 10^{1}~10^{2}, the amplitude will continuously decrease as the input frequency increases.

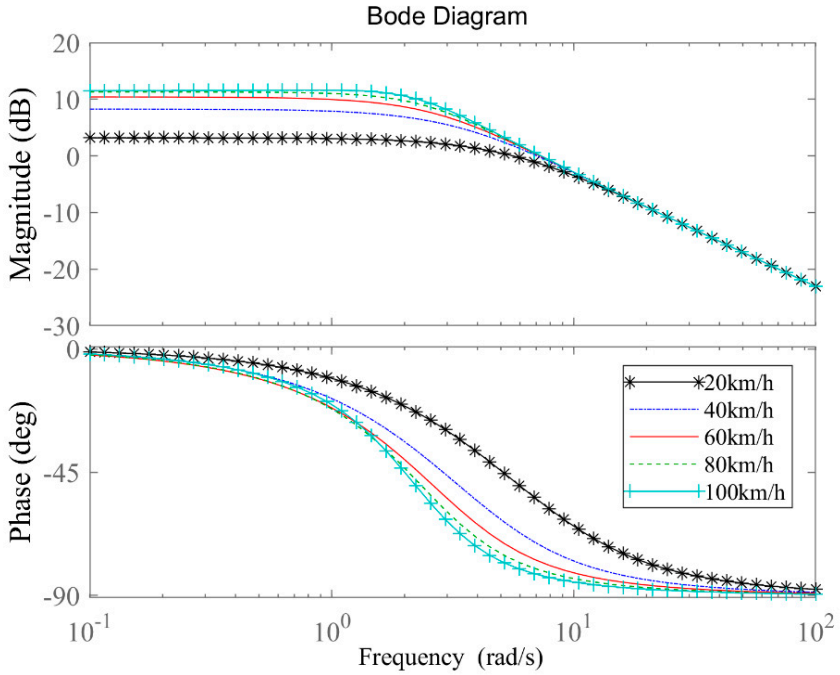


Figure 11. Frequency domain characteristic curves of the vehicle's yaw rate at different speeds.

In Bode plots, the most commonly used physical quantity to analyze system stability is phase margin. Phase margin refers to the sum of the corresponding phase angle and $-180°$ when the amplitude-frequency curve crosses the 0 dB line in the frequency re-

sponse curve. Phase margin can be used to determine the stability and degree of stability of a system. In Figure 11, it can be seen that the phase margins corresponding to these different vehicle speeds are all greater than 0, indicating that the vehicle system is stable. Through more detailed comparison, it was found that as the vehicle speed increases, the corresponding phase margin gradually decreases, indicating that an increase in vehicle speed will reduce the stability of the system. This is consistent with the analysis results of the root locus method.

In order to illustrate the effect of steering center distance l_R on the amplitude-frequency characteristics and phase-frequency characteristics of the yaw rate and the centroid sideslip angle, this section takes different steering center distances l_R for the simulation and analysis under the working condition of the vehicle speed of 100 km/h.

As shown in Figure 12, the Bode plot of the vehicle's yaw rate for different steering center distances is shown. From the figure, it can be seen that, as the steering center distance l_R increases, the gain of the yaw rate decreases; i.e., the steering sensitivity decreases and the stability of the vehicle is improved. The increase of l_R has almost no change on the hysteresis of phase angle. However, it can be seen that its phase margin increases with the increase of l_R, i.e., the stability of vehicle operation is improved.

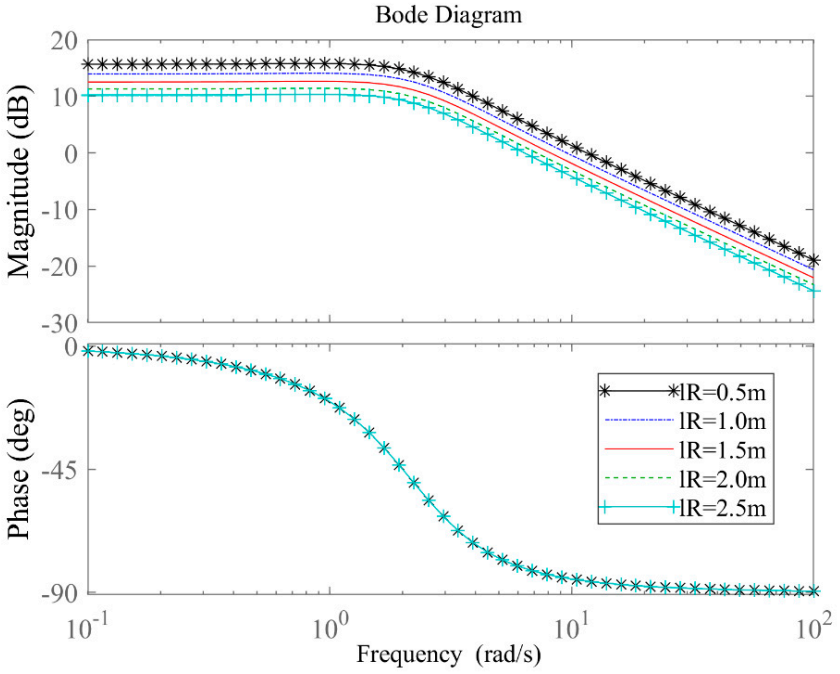


Figure 12. Frequency domain characteristic curves of vehicle's yaw rate for different steering center distances.

4.4. Time Domain Analysis

In order to further analyze the transient response characteristics of the vehicle, in this section, the time-domain characteristics of the yaw rate are simulated under the steering angle step condition (0~10°).

As shown in Figure 13, the time-domain characteristic curves of the vehicle's yaw rate under different vehicle speeds are shown. From the figure, it can be seen that, with the increase in vehicle speed, the maximum yaw rate is larger, and the overshoot is also larger, but the reaction time to reach the steady state value is also longer. That is, the increase in vehicle speed will make the vehicle stability worse.

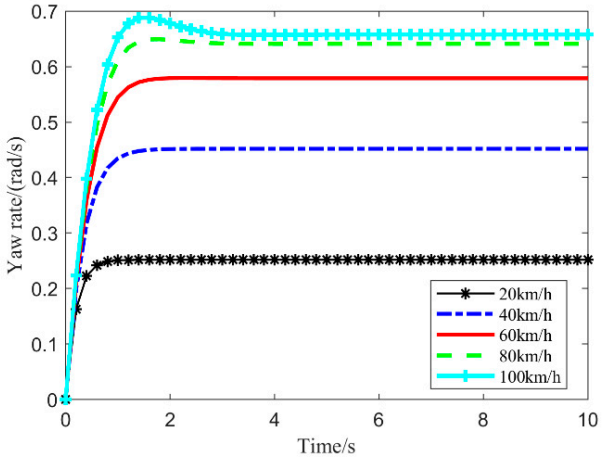


Figure 13. Time-domain characteristic curves of vehicle's yaw rate at different vehicle speeds.

As shown in Figure 14, the time-domain characteristic curves of the vehicle's yaw rate under different steering center distances are shown. From the figure, it can be clearly seen that with the increase in the steering center distance l_R, that is, the steering center moves back, the smaller the vehicle's yaw rate, the smaller the overshoot. That is to say, an appropriate increase in the steering center distance is beneficial to the stability of the vehicle. However, the change in steering center distance has little effect on the time to reach the first peak. That is to say, the change in the steering center distance has little effect on the speed of response of the vehicle's yaw rate.

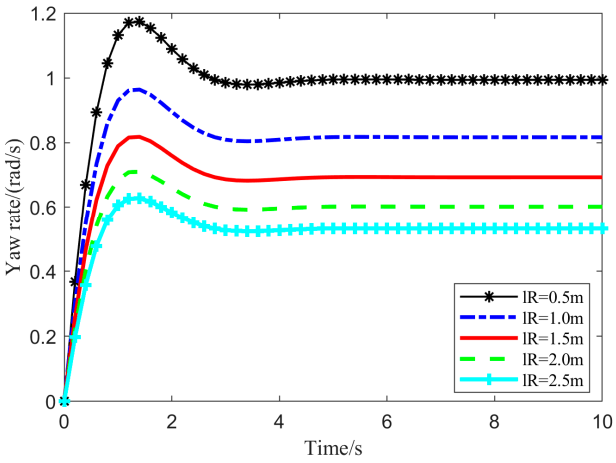


Figure 14. Time-domain characteristic curves of vehicle's yaw rate for different steering center distances.

As shown in Figure 15, the time-domain characteristic curves of the vehicle's yaw rate under different tire sideslip stiffnesses are shown. From the figure, it can be obtained that, in the process of increasing the tire sideslip stiffness from 100,000 to 300,000, the vehicle's yaw rate is also increasing, the overshooting amount is decreasing, the reaction time to reach the steady state of yaw rate is also decreasing, and the time to reach the first peak value is also decreasing. This indicates that within the range of suitable tire sideslip stiffness, increasing the tire sideslip stiffness appropriately is beneficial to the stability and response speed of the system.

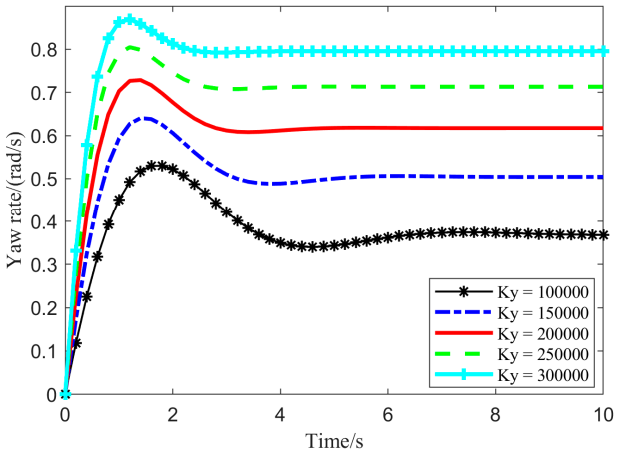


Figure 15. Time-domain characteristic curves of vehicle's yaw rate for different tire sideslip stiffnesses.

4.5. Summary and Suggestions

After analyzing the transient characteristics of the vehicle in this section, the following can be concluded: 1. The four-axle vehicle system constructed in this article is stable, but the system stability deteriorates with increasing vehicle speed. 2. The change in steering center distance has little effect on the response speed of vehicle yaw rate, but increasing the steering center distance is more beneficial for vehicle driving stability. 3. Increasing the tire sideslip stiffness slightly can accelerate the system response speed. Therefore, we recommend that manufacturers of four-axle vehicles increase the steering center distance reasonably, configure tire sideslip stiffness reasonably, and ensure a balanced distribution of response speed and stability.

5. Equivalent Modeling for a Four-Axle Vehicle

5.1. Equivalent Modeling Description

Multi-axle vehicles are often used for specific tasks, such as military, long-distance transport, logistics, and public transport, and play a very important role [1,24]. Therefore, the issue of safety and stability of multi-axle vehicles has become a top research priority. In order to analyze the response characteristics of a four-axle vehicle or even an n ($n > 4$) axle vehicle more easily and efficiently, in this section, the monorail model of a four-axle vehicle will be equated to the monorail model of a conventional two-axle vehicle by using the equivalent modeling method, and the optimal solution will be solved by using several different methods. The effectiveness and accuracy of the equivalent modeling will also be compared in the dimensions of frequency and time domain characteristics.

As shown in Figure 16, a single-track model of a four-axle vehicle is shown. It is assumed at this point that a classical two-axle monorail model can be obtained by using an equivalent front axle to represent the front two axles of the vehicle and an equivalent rear axle to represent the rear two axles of the vehicle, which is more useful for analyzing the response characteristics of the vehicle.

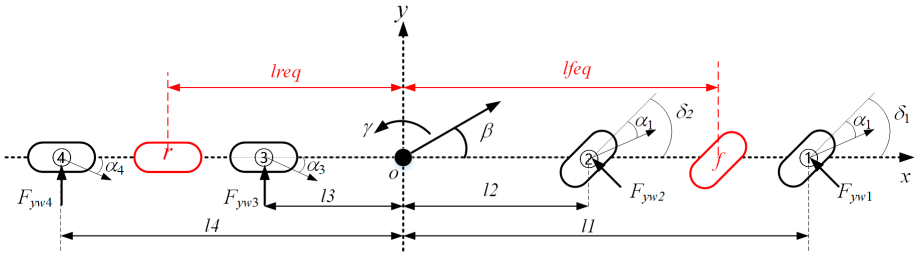


Figure 16. Four-axle vehicle monorail model and equivalent model derivation.

Such an equivalence can ensure that the forces and moments of the equivalent model at the center of mass O are kept constant, and therefore the approximate consistency of the response characteristics of the equivalent model can also be ensured. Meanwhile, four equivalent parameters l_{feq}, K_{feq}, l_{req}, and K_{req} are introduced in the derivation process of the model equivalence, which is the displacement from the equivalent front axle to the center of mass, the tire sideslip stiffness of the equivalent front axle, the displacement from the equivalent rear axle to the center of mass and the tire sideslip stiffness of the equivalent rear axle, respectively. Their lateral equations of motion are obtained according to the four-axis monorail model and the equivalent model in Figure 16, respectively:

$$m(\dot{v}+\gamma u) = K_1\left(\delta_1-\beta-\frac{l_1\gamma}{u}\right)+K_2\left(N\delta_1-\beta-\frac{l_2\gamma}{u}\right)+K_3\left(-\beta-\frac{l_3\gamma}{u}\right)+K_4\left(-\beta-\frac{l_4\gamma}{u}\right) \tag{38}$$

$$m(\dot{v}+\gamma u) = K_{feq}\left(\delta_1-\beta-\frac{l_{feq}\gamma}{u}\right)+K_{req}\left(-\beta-\frac{l_{req}\gamma}{u}\right) \tag{39}$$

where l_{feq}, K_{feq}, l_{req}, and K_{req} are the displacement from the equivalent front axle to the center of mass, the tire sideslip stiffness of the equivalent front axle, the displacement from the equivalent rear axle to the center of mass and the tire sideslip stiffness of the equivalent rear axle, respectively.

Similarly, the equations of motion of the yaw can be obtained for the four-axis monorail model and the equivalent model, respectively:

$$I_{zz}\dot{\gamma} = l_1K_1\left(\delta_1-\beta-\frac{l_1\gamma}{u}\right)+l_2K_2\left(N\delta_1-\beta-\frac{l_2\gamma}{u}\right)+l_3K_3\left(-\beta-\frac{l_3\gamma}{u}\right)+l_4K_4\left(-\beta-\frac{l_4\gamma}{u}\right) \tag{40}$$

$$I_{zz}\dot{\gamma} = l_{feq}K_{feq}\left(\delta_1-\beta-\frac{l_{feq}\gamma}{u}\right)+l_{req}K_{req}\left(-\beta-\frac{l_{req}\gamma}{u}\right) \tag{41}$$

According to the basic principles of vehicle dynamics, the forces and moments at the center of mass O determine the kinematic properties of the vehicle. Therefore, in order to make the kinematic characteristics of the four-axis vehicle model consistent with the equivalent two-axis model, we need to keep the lateral force and the yaw moment at the center of mass O equal for both models. That is, the coupled Equations (38)–(41) are obtained:

$$\begin{aligned}(K_1+NK_2)\delta_1-(K_1+K_2+K_3+K_4)\beta-(K_1l_1+K_2l_2+K_3l_3+K_4l_4)\tfrac{\gamma}{u}\\ =K_{feq}\delta_1-\left(K_{feq}+K_{req}\right)\beta-\left(K_{feq}l_{feq}+K_{req}l_{req}\right)\tfrac{\gamma}{u}\end{aligned} \tag{42}$$

$$\begin{aligned}(l_1K_1+Nl_2K_2)\delta_1-(l_1K_1+l_2K_2+l_3K_3+l_4K_4)\beta-\left({l_1}^2K_1+{l_2}^2K_2+{l_3}^2K_3+{l_4}^2K_4\right)\tfrac{\gamma}{u}\\ =l_{feq}K_{feq}\delta_1-\left(l_{feq}K_{feq}+l_{req}K_{req}\right)\beta-\left(K_{feq}{l_{feq}}^2+K_{req}{l_{req}}^2\right)\tfrac{\gamma}{u}\end{aligned} \tag{43}$$

5.2. Equalization Methods

The parametric equations for the equivalent front and equivalent rear axles can be obtained by associating Equations (42) and (43), respectively:

$$\begin{cases}K_{feq}=K_1+NK_2\\ l_{feq}K_{feq}=l_1K_1+Nl_2K_2\\ {l_{feq}}^2K_{feq}={l_1}^2K_1+N{l_2}^2K_2\end{cases} \tag{44}$$

$$\begin{cases}K_{req}=(1-N)K_2+K_3+K_4\\ l_{req}K_{req}=(1-N)l_2K_2+l_3K_3+l_4K_4\\ {l_{req}}^2K_{req}=(1-N){l_2}^2K_2+{l_3}^2K_3+{l_4}^2K_4\end{cases} \tag{45}$$

Equation (44) is the parametric equation of K_{feq} and l_{feq} of the equivalent front bridge. In order to find the optimal solution of these two equivalent parameters, this paper represents l_{feq} as the x-axis and K_{feq} as the y-axis, and plots the three curves of the function. As shown

in Figure 17, the three curves cannot intersect at the same point at the same time, but they can form a region of an approximate triangle, which is the optimal region for solving the optimal point.

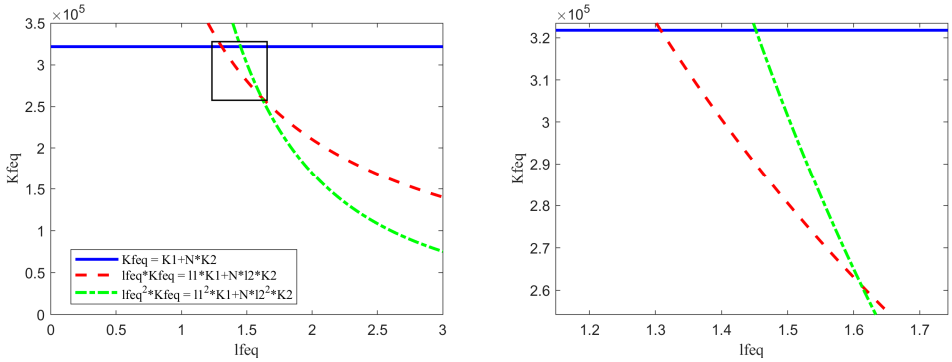


Figure 17. Equivalent front bridge optimal region.

Similarly, *Iraq* can be represented as the *x*-axis and K_{req} as the *y*-axis, and the curves of the three functions are plotted. The optimal region of the approximate triangle can also be obtained as shown in Figure 18.

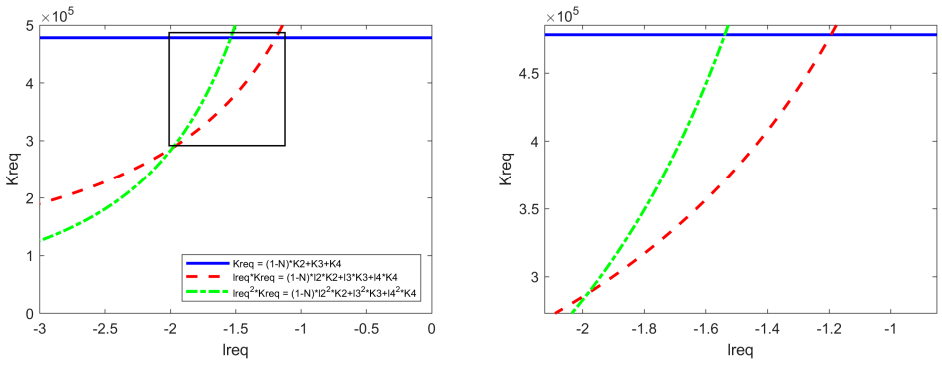


Figure 18. Equivalent rear axle optimum region.

5.2.1. Equalization Based on CG Method

Therefore, in order to find the equivalent front axle parameters l_{feq} and K_{feq}, it is necessary to find the optimal point in the optimal region. Yubiao Zhang [10] found that the center of gravity of the approximate triangle as the solution point can achieve a relatively good equivalent effect in the equivalent rear axle of a three-axle vehicle. Here, in this paper, we also try to use the center of gravity of the approximate triangle as the solution point, and carry out simulation analysis and discussion.

As shown in Figure 19, *P*1, *P*2, and *P*3 are the intersection points of the three curves, and the center of gravity is the midline of the three sides of the triangle, assuming that point P is the center of gravity of the approximate triangle. According to Equation (44), the intersection points of the three curves are as follows:

$$P_1(x1, y1) = \left(\frac{l_1 K_1 + N l_2 K_2}{K_1 + N K_2}, K_1 + N K_2 \right) \tag{46}$$

$$P_2(x2, y2) = \left(\sqrt{\frac{{l_1}^2 K_1 + N {l_2}^2 K_2}{K_1 + N K_2}}, K_1 + N K_2 \right) \tag{47}$$

$$P_3(x3, y3) = \left(\frac{{l_1}^2 K_1 + N {l_2}^2 K_2}{l_1 K_1 + N l_2 K_2}, \frac{(l_1 K_1 + N l_2 K_2)^2}{{l_1}^2 K_1 + N {l_2}^2 K_2} \right) \tag{48}$$

where x_1 and y_1 represent the horizontal and vertical coordinates of point P_1; x_2, and y_2 represent the horizontal and vertical coordinates of point P_2; and x_3 and y_3 represent the horizontal and vertical coordinates of point P_3.

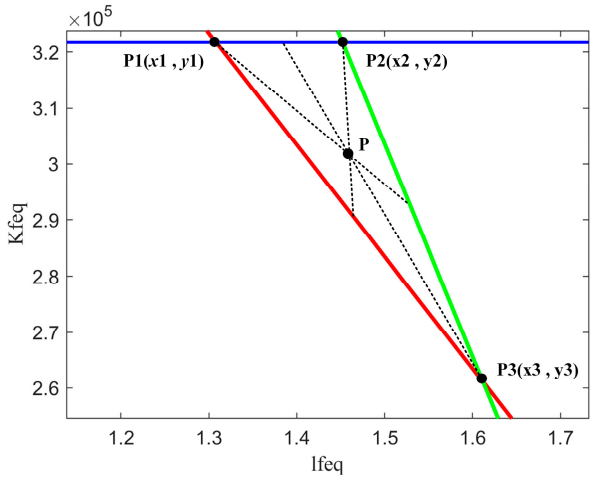


Figure 19. Equivalent front axle optimum point solution.

The coordinates of point P and the parameters related to the equivalent front axis can be obtained by the center of gravity solution formula of the approximate triangle, as shown in Equations (49)–(51):

$$\begin{bmatrix} x \\ y \end{bmatrix} = \begin{bmatrix} \frac{(x_1+x_2+x_3)}{3} \\ \frac{(y_1+y_2+y_3)}{3} \end{bmatrix} \tag{49}$$

$$l_{feq} = \frac{1}{3}\left(\frac{l_1K_1 + Nl_2K_2}{K_1 + NK_2} + \sqrt{\frac{{l_1}^2K_1 + N{l_2}^2K_2}{K_1 + NK_2}} + \frac{{l_1}^2K_1 + N{l_2}^2K_2}{l_1K_1 + Nl_2K_2} \right) \tag{50}$$

$$K_{feq} = \frac{1}{3}\left(2K_1 + 2NK_2 + \frac{(l_1K_1 + Nl_2K_2)^2}{{l_1}^2K_1 + N{l_2}^2K_2} \right) \tag{51}$$

The equivalent posterior axis solution process based on the center of gravity of the approximate triangle is also similar, as shown in Figure 20. Q1, Q2, and Q3 are the intersection points of the three curves, assuming that point P is the center of gravity of the approximate triangle. According to Equation (44), the intersection points of the three curves can be found to be as follows:

$$Q_1(m_1, n_1) = \left(\frac{(1-N)l_2K_2 + l_3K_3 + l_4K_4}{(1-N)K_2 + K_3 + K_4},\ (1-N)K_2 + K_3 + K_4 \right) \tag{52}$$

$$Q_2(m_2, n_2) = \left(\sqrt{\frac{(1-N){l_2}^2K_2 + {l_3}^2K_3 + {l_4}^2K_4}{(1-N)K_2 + K_3 + K_4}},\ (1-N)K_2 + K_3 + K_4 \right) \tag{53}$$

$$Q_3(m_3, n_3) = \left(\frac{(1-N){l_2}^2K_2 + {l_3}^2K_3 + {l_4}^2K_4}{(1-N)l_2K_2 + l_3K_3 + l_4K_4}, \frac{[(1-N)l_2K_2 + l_3K_3 + l_4K_4]^2}{(1-N){l_2}^2K_2 + {l_3}^2K_3 + {l_4}^2K_4} \right) \tag{54}$$

where m_1 and n_1 represent the horizontal and vertical coordinates of point P_1; m_2 and n_2 represent the horizontal and vertical coordinates of point P_2; and m_3 and n_3 represent the horizontal and vertical coordinates of point P_3.

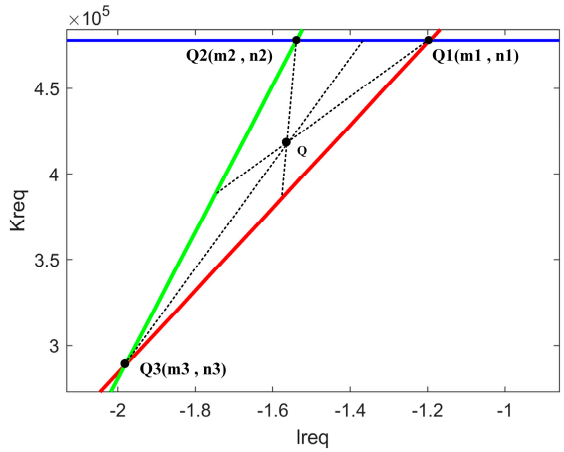


Figure 20. Equivalent rear axial convex optimization solution.

The parameters related to the equivalent posterior axis can be found through the center of gravity solution formula of the approximate triangle, as shown in Equations (55) and (56):

$$\begin{cases} l_{req} = \frac{1}{3}\left(\frac{bo}{ao} + \sqrt{\frac{co}{ao}} + \frac{co}{bo}\right) \\ K_{req} = \frac{1}{3}\left(2ao + \frac{bo^2}{co}\right) \end{cases} \tag{55}$$

$$\begin{cases} ao = (1-N)K_2 + K_3 + K_4 \\ bo = (1-N)l_2K_2 + l_3K_3 + l_4K_4 \\ co = (1-N){l_2}^2K_2 + {l_3}^2K_3 + {l_4}^2K_4 \end{cases} \tag{56}$$

Figures 21 and 22 show the comparative effect of the time and frequency domains based on the center of gravity equivalent. As can be seen from the figures, the system of its equivalent model is stable, but the overall trend of the curve is slightly different from that of the original model, and the amplitude at the time of stability is slightly smaller than that of the original model. Therefore, from the perspective of comparative analysis, the equivalent results of the four-axle vehicle based on the center of gravity are not impressive. The reason may be that the optimal region of the equivalent front axle and equivalent rear axle is too large, which leads to the solution point cannot satisfy the demand of equivalent stiffness and equivalent wheelbase at the same time. So other methods need to be tried.

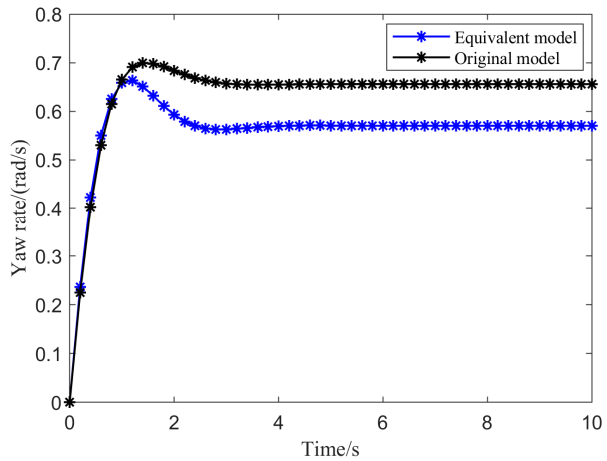


Figure 21. Equivalent comparison of time-domain characteristics of transverse pendulum angular velocity.

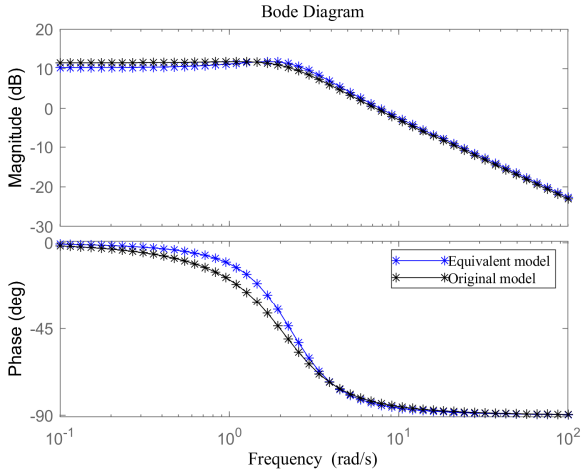


Figure 22. Equivalent comparison of frequency domain characteristics of transverse pendulum angular velocity.

5.2.2. Equalization Based on Compensation Points Method

Through the previous analysis, it can be seen that the equivalent parameter solution based on the center of gravity is not obvious for the equivalent effect of the four-axle vehicle, which can not meet the demand of equivalent stiffness and equivalent axle spacing, so here we will try to use the compensation point for the solution. That is, the solution point of the equivalent front axle should be able to compensate for the solution point of the equivalent rear axle, and in turn, the solution point of the equivalent rear axle can also compensate for the solution point of the equivalent front axle.

Therefore, according to the compensation principle, the solution point of the equivalent front axle is taken as point P3, which fully satisfies the requirement of equivalent axle distance and ignores part of the requirement of equivalent stiffness. Then, take the solution point of the equivalent rear axle as point Q1, which completely meets the demand for equivalent stiffness and ignores part of the demand for an equivalent wheelbase. In this way, the equivalent front axle and equivalent rear axle parameters can be obtained:

$$\begin{cases} l_{feq} = x_3 \\ K_{feq} = y_3 \\ l_{req} = m_1 \\ K_{req} = n_1 \end{cases} \tag{57}$$

5.2.3. Equalization Based on Outer Center Method

The exocentre of a triangle is the intersection of the perpendicular bisectors of the three sides, and it is characterized by the fact that this intersection is equidistant from the vertices. Since this property may be able to better distribute the demand for the intersection of the three equivalent curves equally at the same time, in order to find the optimal point of the equivalence, this paper will also try to use the epicenter of the approximate triangle as a solution point. Assuming that, the outer center of the equivalent front bridge is W, then $|P_1W| = |P_2W|$, $|P_1W| = |P_3W|$, the equivalent front bridge parameters can be obtained, and similarly, the equivalent back bridge parameters can also be obtained:

$$l_{feq} = \frac{{x_2}^2 - {x_1}^2 + {y_2}^2 - {y_1}^2}{2x_2 - 2x_1} \tag{58}$$

$$K_{feq} = \frac{{x_3}^2 - {x_1}^2 + {y_3}^2 - {y_1}^2 - (2x_3 - 2x_2)l_{feq}}{2y_3 - 2y_1} \tag{59}$$

$$l_{req} = \frac{{m_2}^2 - {m_1}^2 + {n_2}^2 - {n_1}^2}{2m_2 - 2m_1} \tag{60}$$

$$K_{req} = \frac{{m_3}^2 - {m_1}^2 + {n_3}^2 - {n_1}^2 - (2m_3 - 2m_2)l_{req}}{2n_3 - 2n_1} \tag{61}$$

5.2.4. Equalization Based on Inner Method

The inner core of a triangle is the point of intersection of the angle bisectors of the three interior angles, and it is characterized by the fact that the distance from this point of intersection to the three sides is equal. Since this property may be able to better distribute the demand of the three equivalent curves equally, in order to find out the optimal point of equivalence, this paper will try to use the inner part of the approximate triangle as the solution point. Also, the equivalent front bridge and equivalent back bridge parameters can be obtained from the coordinate formulae of the inner triangle:

$$l_{feq} = \frac{ax_1 + bx_2 + cx_3}{a + b + c} \tag{62}$$

$$K_{feq} = \frac{ay_1 + by_2 + cy_3}{a + b + c} \tag{63}$$

$$l_{req} = \frac{q_1m_1 + q_2m_2 + q_3m_3}{q_1 + q_2 + q_3} \tag{64}$$

$$K_{req} = \frac{q_1n_1 + q_2n_2 + q_3n_3}{q_1 + q_2 + q_3} \tag{65}$$

where a, b, and c denote the equivalent front bridge approximate triangular side lengths P_2P_3, P_1P_3, and P_1P_2, respectively; q_1, q_2, and q_3 denote the equivalent rear bridge approximate triangular side lengths Q_2Q_3, Q_1Q_3, and Q_1Q_2, respectively.

5.3. Equivalent Model Derivation

In order to compare and analyze the difference between the response characteristics of the equivalent model and the original model, it is necessary to construct the monorail model of the equivalent model. The equation of state of the single-track model of the equivalent model is obtained from (28) and (40):

$$\begin{bmatrix} \dot{\beta} \\ \dot{\gamma} \end{bmatrix} = \begin{bmatrix} -\frac{K_{feq}+K_{req}}{mu} & -1 - \frac{K_{feq}l_{feq}+K_{req}l_{req}}{mu^2} \\ -\frac{K_{feq}l_{feq}+K_{req}l_{req}}{I_{zz}} & -\frac{K_{feq}{l_{feq}}^2+K_{req}{l_{req}}^2}{I_{zz}u} \end{bmatrix} \begin{bmatrix} \beta \\ \gamma \end{bmatrix} + \begin{bmatrix} \frac{K_{feq}}{mu} \\ \frac{K_{feq}l_{feq}}{I_{zz}} \end{bmatrix} \delta_1 \tag{66}$$

For ease of calculation, Equation (66) is simplified to the following equation:

$$\begin{cases} \dot{\beta} = a_{11}\beta + a_{12}\gamma + b_{11}\delta_1 \\ \dot{\gamma} = a_{21}\beta + a_{22}\gamma + b_{21}\delta_1 \end{cases} \tag{67}$$

where $a_{11} = -\frac{K_{feq}+K_{req}}{mu}$; $a_{12} = -1 - \frac{K_{feq}l_{feq}+K_{req}l_{req}}{mu^2}$; $b_{11} = \frac{K_{feq}}{mu}$; $a_{21} = -\frac{K_{feq}l_{feq}+K_{req}l_{req}}{I_{zz}}$; $a_{22} = -\frac{K_{feq}{l_{feq}}^2+K_{req}{l_{req}}^2}{I_{zz}u}$; and $b_{21} = \frac{K_{feq}l_{feq}}{I_{zz}}$.

The Laplace transform of Equation (67) yields the following:

$$\begin{cases} (s - a_{11})\beta(s) - a_{12}\gamma_{(s)} - b_{11}\delta_{1(s)} = 0 \\ a_{21}\beta(s) + (a_{22} - s)\gamma_{(s)} + b_{21}\delta_{1(s)} = 0 \end{cases} \tag{68}$$

The dissipative solution of Equation (68) yields the transfer function of the yaw rate and the centroid sideslip angle for the equivalent model as follows:

$$G_{\gamma eq(s)} = \frac{\gamma_{eq(s)}}{\delta_{1(s)}} = \frac{b_{21}s + a_{21}b_{11} - a_{11}b_{21}}{s^2 - (a_{11} + a_{22})s + a_{11}a_{22} - a_{21}a_{12}} \tag{69}$$

$$G_{\beta eq(s)} = \frac{\beta_{eq(s)}}{\delta_{1(s)}} = \frac{b_{11}s + b_{21}a_{12} - b_{11}a_{22}}{s^2 - (a_{11} + a_{22})s + a_{11}a_{22} - a_{21}a_{12}} \tag{70}$$

Letting the Laplace variable $s = 0$, the steady-state gains of the equivalent model yaw rate and the centroid sideslip angle against the steering angle δ_1 are obtained, respectively:

$$G_{\gamma sseq} = \frac{a_{21}b_{11} - a_{11}b_{21}}{a_{11}a_{22} - a_{21}a_{12}} \tag{71}$$

$$G_{\beta sseq} = \frac{b_{21}a_{12} - b_{11}a_{22}}{a_{11}a_{22} - a_{21}a_{12}} \tag{72}$$

5.4. Comparative Analysis

The comparison curves of the time-domain characteristics of the equivalent model based on the triangular center of gravity, outer center, inner center, and compensation point with the original model are shown in Figure 23. It can be seen from the figures that the systems of these four methods are stable, and the system response time and the basic trend of the plots are basically the same as that of the original model. However, there is a certain gap with the original model in terms of overshooting amount, adjustment time, and peak time.

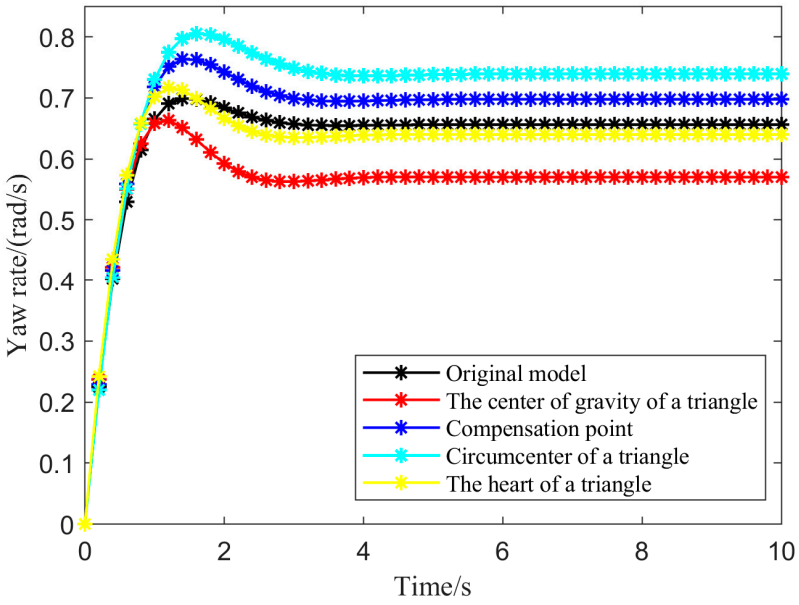


Figure 23. Comparison of the time domain characteristics of the yaw rate with different equivalent methods.

Based on the above figure and Table 2 analysis, first of all, in terms of the amount of overshooting, the amount of overshooting of these four equivalence methods is slightly larger than the original model overshooting, especially the equivalence based on the triangular center of gravity, which has the largest amount of overshooting of the system, followed by the outer center, the compensating point, and the inner center, respectively, and the smallest amount of overshooting is still the original model. So, it will cause a certain lack of system stability during the equivalence process. Secondly, in terms of reaching the steady state worth adjustment time, these methods are not much different from the original model, and the adjustment time based on the inner heart of the triangle is consistent with the original model. It can be seen that the effect of equivalence on the adjustment time of the system is small. Then, the time for the system to reach the peak value is also not much different from the original model. Then, in terms of steady-state values, the smallest difference is in the equivalent method based on the inner triangle, which is only slightly smaller than the original model. The steady-state values of all other equivalent methods

have a large gap compared with the original model. It can be seen that the equivalence still has a large effect on the steady-state value of the system. Finally, the response times of the four equivalent methods are consistent with the original model, and the effect of equivalence on the system response time is almost negligible.

Table 2. Comparison of step response performance characteristics.

Methods/Indicators	Overshoot	Adjustment Time	Peak Time	Steady-State Value	Response Time
Original model	6.6%	5 s	1.4 s	0.656	unanimous
Gravity	16.4%	5.4 s	1.2 s	0.570	unanimous
Recompense point	9.4%	5.4 s	1.4 s	0.698	unanimous
Triangle core	8.9%	6 s	1.6 s	0.739	unanimous
Inner triangle	11.9%	5 s	1.2 s	0.640	unanimous

The comparison curves of the frequency domain characteristics of the equivalent models based on the triangular center of gravity, outer center, inner center, and compensation point with the original model are shown in Figure 24. From the figure, it can be seen that with the change in frequency, the magnitude of the system gain and the trend of the phase change in these four methods are basically consistent with the original model. However, from a more detailed observation, it is found that the trends of the gain and phase of the equivalent method based on the inner part of the triangle most closely match those of the original model.

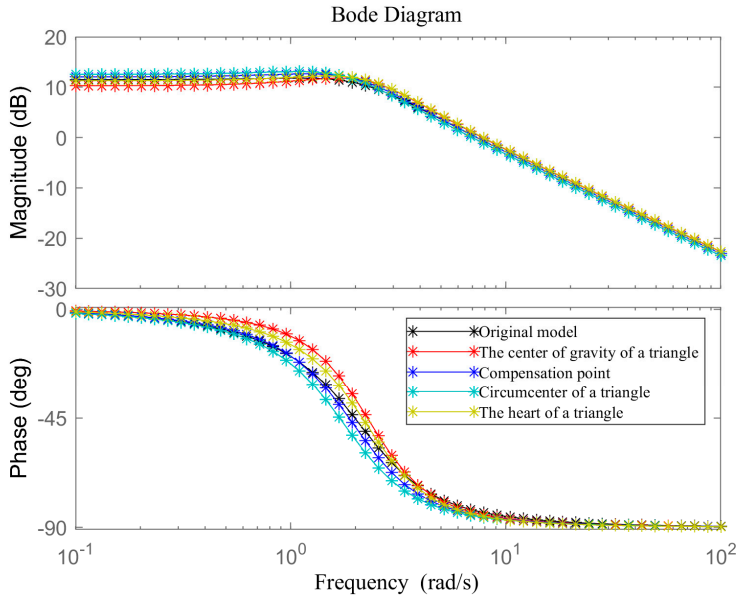


Figure 24. Comparison of the frequency domain characteristics of the yaw rate for different equivalent methods.

In summary, among the equivalent methods for equivalent modeling of four-axle vehicles. The equivalent method based on the triangle core proposed in this paper is superior to the equivalent method based on the center of gravity of approximate triangles proposed by Yubiao Zhang. The response characteristics and performance indexes in various aspects are more in line with the characteristics of the original model. The method proposed in this article tends to be more inclined towards finding the optimal solution. In equivalent modeling of vehicles with other axle numbers, the method proposed in this article may not be the optimal solution.

6. Conclusions

Taking the four-axis vehicle as the research object, this paper mainly analyses the steady state characteristics, transient characteristics, and stability of the four-axis vehicle, as well as the equivalent modeling and verification of the four-axis vehicle using the principle of equivalence.

Firstly, a linear two-degree-of-freedom model of the four-axis vehicle was established, and the mathematical transfer function expressions for the yaw rate and the centroid sideslip angle were deduced on the basis of the model. The steady-state parameters such as steady state yaw rate gain $G_{\gamma ss}$, steady state centroid sideslip angle gain $G_{\beta ss}$, stability factor K_n, equivalent axial distance l_n, and equivalent centroid sideslip angle coefficient $K_{n'}$ were obtained by using the transfer functions.

Secondly, the steady state parameters were analyzed as affected by the parameters of vehicle speed u, tire sideslip stiffness K_y, and steering center distance l_R. The corresponding conclusions were obtained: (1) The four-axle vehicle has understeer characteristics. (2) At high speeds, a little increase in the stability factor K_n, i.e., a larger amount of understeer, will help the vehicle's sideslip stability. (3) A higher tire sideslip stiffness at low speeds is beneficial to the steering sensitivity of the vehicle. At high speeds, a lower tire stiffness is better for overall stability. (4) The steering center of the vehicle is set back a bit, which is more beneficial to the overall stability of the vehicle.

Then, in the transient analysis, this paper gives a detailed derivation and analytical description of the transient parameters of the four-axis vehicle from the perspectives of complex domain, frequency domain, and time domain. The corresponding conclusions are obtained: (1) The root trajectory diagram, Bode diagram, and step response of the system all prove the stability of the system. (2) Parameters, such as vehicle speed u, steering center distance l_R, and tire sideslip stiffness K_y will not change the stability of the system completely, but they will affect the stability of the system.

Finally, in order to be able to analyze four-axle vehicles and n-axle vehicles more conveniently and efficiently, this paper uses equivalent modeling to simplify four-axle vehicles into traditional two-axle vehicles, and proposes an optimal solution method based on the inner heart of the approximation triangle, the outer heart, and the compensation point, and compares it with the equivalent method based on the center of gravity of the approximation triangle. The solution method based on the inner center of the approximate triangle is found to be the most suitable for four-axis vehicles.

Author Contributions: D.Z. and W.L. conceived and designed the research; Y.Y., Y.H. and P.Z. prepared the MGR; W.L., D.X. and G.C. conducted the evaluation experiments and analyzed the experimental data; H.F. and L.G. review and editing the data. All authors wrote the manuscript. All authors have read and agreed to the published version of the manuscript.

Funding: This work was supported in part by the Natural Science Foundation of Jiangxi Province (Grant No.20232BAB214092), The Ganpo Talent Support Program-Leading Academic and Technical Personnel in Major Disciplines of Jiangxi Province (Grant No.20232BCJ23091), the National Natural Science Foundation of China (Grant No. 52462053), the Natural Science Foundation of Jiangxi Province (Grant No.20224BAB214045), the Select the Best Candidates to Undertake Key Research Projects of Nanchang City (Grant No. 2023JBGS003), the Science and technology research project of Jiangxi Provincial Department of Education (Grant No. GJJ2200662), and The 03 Special Program and 5G Project of Jiangxi Province (Grant No.20232ABC03A30).

Data Availability Statement: All data needed to evaluate the conclusions in the paper are present in the paper.

Acknowledgments: The authors would like to acknowledge the support from the Institute of Intelligent Manufacturing and Precision Machining of East China Jiaotong University.

Conflicts of Interest: All authors declare that they have no conflicts of interest or financial conflicts to disclose.

References

1. Wang, W.; Li, J.; Li, X.; Li, Z.; Guo, N. Multi-Objective Collaborative Control Method for Multi-Axle Distributed Vehicle Assisted Driving. *Appl. Sci.* **2023**, *13*, 7769. [CrossRef]
2. Liu, Q.; Du, H.; Yu, Y.; Huang, H.; Wang, Y.; Fang, J. Research on active safety control for heavy multi-axle vehicles under steering system failure. *Proc. Inst. Mech. Engineers. Part D J. Automob. Eng.* **2023**, *238*, 2544–2556. [CrossRef]
3. Li, Z.; Li, J.; Min, Q.; Liu, B. A Fast-Computing Path Tracking Control Strategy for Autonomous Multi-Axle Electric Vehicle Considering Safety and Stability. *IEEE Trans. Transp. Electrif.* **2023**, *10*, 6024–6038. [CrossRef]
4. Deng, Z.W.; Zhao, Q.X.; Zhao, Y.Q.; Wang, B.H.; Gao, W.; Kong, X.X. Active LQR multi-axle-steering method for improving maneuverability and stability of multi-trailer articulated heavy vehicles. *Int. J. Automot. Technol.* **2022**, *23*, 939–955. [CrossRef]
5. Xu, T.; Liu, X.; Li, Z.; Feng, B.; Ji, X.; Wu, F. A Sliding Mode Control Scheme for Steering Flexibility and Stability in All-wheel-steering Multi-Axle Vehicles. *Int. J. Control. Autom. Syst.* **2023**, *21*, 1926–1938. [CrossRef]
6. Zhang, Z.; Du, H.; Chen, S.; Li, Y.; Wang, H. A novel electro-hydraulic servo steering system for Ackermann steering of heavy multi-axle vehicle. *Proc. Inst. Mech. Engineers. Part D J. Automob. Eng.* **2022**, *236*, 2610–2624. [CrossRef]
7. Gao, L.; Gao, Q.H.; Cheng, H.J.; Liu, Z.H.; He, X.L. Multi-body modeling and dynamic analysis of the heavy-load multi-axle vehicle Based on 6S/6M ABS control. *Proc. Inst. Mech. Engineers. Part D J. Automob. Eng.* **2022**, *238*, 491–508. [CrossRef]
8. Zhang, Y.; Huang, Y.; Wang, H.; Khajepour, A. A comparative study of equivalent modelling for multi-axle vehicle. *Veh. Syst. Dyn.* **2018**, *56*, 443–460. [CrossRef]
9. Zhang, Y.; Khajepour, A.; Huang, Y. Multi-axle/articulated bus dynamics modeling: A reconfigurable approach. *Veh. Syst. Dyn.* **2018**, *56*, 1315–1343. [CrossRef]
10. Zhang, Y. Multi-axle vehicle modeling and stability control: A reconfigurable approach. Ph.D. Thesis, University of Waterloo, Waterloo, ON, Canada, 2019.
11. Williams, D.E. On the equivalent wheelbase of a three-axle vehicle. *Veh. Syst. Dyn.* **2011**, *49*, 1521–1532. [CrossRef]
12. Williams, D.E. Generalised multi-axle vehicle handling. *Veh. Syst. Dyn.* **2012**, *50*, 149–166. [CrossRef]
13. Wu, Z.C.; Chen, C. Handling stability of three-axle vehicle with dual-front-axle-steering system. *J. Jiangsu Univ. Nat. Sci. Ed.* **2016**, *37*, 640–644.
14. Yao, G.L.; Wang, B.H. Analysis and Research on Steering Mode of Multi-Axle Steering Commercial Vehicle. *J. Hubei Univ. Automot. Technol.* **2018**, *32*, 27G31.
15. Ding, J.; Guo, K. Development of a generalised equivalent estimation approach for multi-axle vehicle handling dynamics. *Veh. Syst. Dyn.* **2016**, *54*, 20–57. [CrossRef]
16. Ahmed, W.; Azim, R.A.; Fatima, S. Steering strategy for a multi-axle wheeled vehicles. In Proceedings of the ASME International Mechanical Engineering Congress and Exposition, Pittsburgh, PA, USA, 9–15 November 2018; Volume 52040, p. V04BT06A008.
17. Wang, S.; Zhang, J.; Li, H. Steering performance simulation of three-axle vehicle with multi-axle dynamic steering. In Proceedings of the 2008 IEEE Vehicle Power and Propulsion Conference, Harbin, Chian, 3–5 September 2008; pp. 1–5.
18. Shen, Y.H.; Gao, Y.; Xu, T. Multi-axle vehicle dynamics stability control algorithm with all independent drive wheel. *Int. J. Automot. Technol.* **2016**, *17*, 795–805. [CrossRef]
19. Tong, H.; Gao, Q.; Liu, Z.; Wang, D. Driving Dynamic Characteristics of Multi-Axle Special Vehicles in Shortage of Tires. *J. Shanghai Jiaotong Univ.* **2023**, *57*, 335–344.
20. Sui, D.; Zhang, Y. Analyzation of the Application Scenarios of Ackerman Geometry Based on Vehicle Steering Model. *Highlights Sci. Eng. Technol.* **2023**, *46*, 71–82. [CrossRef]
21. Huang, B.; Yuan, Z.; Peng, D.; Wei, X.; Wang, Y. Coordination Control of Active Steering and Direct Yaw Control for the Articulated Steering Vehicle. *Shock. Vib.* **2023**, *2023*, 5577119. [CrossRef]
22. Fang, P.; Cai, Y.; Chen, L.; Wang, H.; Li, Y.; Sotelo, M.A.; Li, Z. A high-performance neural network vehicle dynamics model for trajectory tracking control. *Proc. Inst. Mech. Eng. Part D J. Automob. Eng.* **2023**, *237*, 1695–1709. [CrossRef]
23. Han, W.; Li, A.; Huang, X.; Li, W.; Cao, J.; Bu, H. Trajectory tracking of in-wheel motor electric vehicles based on preview time adaptive and torque difference control. *Adv. Mech. Eng.* **2022**, *14*, 16878132221089909. [CrossRef]
24. Chen, X.; Guo, K.H. Development for generalised multi-axle steering vehicle handling. *Int. J. Heavy Veh. Syst.* **2020**, *27*, 777–799. [CrossRef]

Disclaimer/Publisher's Note: The statements, opinions and data contained in all publications are solely those of the individual author(s) and contributor(s) and not of MDPI and/or the editor(s). MDPI and/or the editor(s) disclaim responsibility for any injury to people or property resulting from any ideas, methods, instructions or products referred to in the content.